Int. J. Electrochem. Sci., 13 **(2018)** 6717 – 6733, doi: 10.20964/2018.07.26

International Journal of ELECTROCHEMICAL SCIENCE
www.electrochemsci.org

Study of the Corrosion Behaviour of the Steel Q315NS Heat-affected Zone in H_2SO_4 Solution by Electrochemical Noise

Suqiang Zhang[1], *Hongyun Zhao*[1], *Fengyuan Shu*[1,*], *Guodong Wang*[1,2], *Bin Liu*[3] *and Binshi Xu*[4]

[1] Shandong Provincial Key Lab of Special Welding Technology, Harbin Institute of Technology, Harbin 150001, China
[2] State Key Laboratory of Rolling and Automation, Northeastern University, Shenyang 110819, China
[3] School of Materials Science and Engineering, Jiangsu University of Science and Technology, Zhenjiang, 212003, China
[4] National Key Laboratory for Remanufacturing, Academy of Armored Forces Engineering, Beijing 100072, China
[*]E-mail: shufengyuanhit@163.com

Received: 16 February 2018 / *Accepted:* 17 March 2018 / *Published:* 5 June 2018

To provide insight into the influence of the welding thermal cycle on the corrosion behaviour of Q315NS steel, the corrosion behaviours of the base metal (BM) and heat-affected zone (HAZ) in 50 wt.% H_2SO_4 solution at 25 °C were investigated with surface observations, electrochemical noise (EN) measurements, polarization measurements and electrochemical impedance spectroscopy (EIS). The transient characteristics, power spectral density (PSD) and wavelet transform were employed to analyse the EN data. The microstructure of the BM, fine-grained region (FGHAZ) and inter-critical region (ICHAZ) mainly consisted of pearlite and ferrite, while granular bainite was the main phase in the microstructure of the coarse-grained region (CGHAZ). The corrosion processes of the BM, FGHAZ and ICHAZ were similar due to the similar microstructures, while the corrosion process of the CGHAZ was different from the others. A dense corrosion product film was formed on the BM, FGHAZ and ICHAZ, while a uniform, loose and rough corrosion product film was formed on the CGHAZ. The corrosion products of the BM and CGHAZ were both mainly composed of $FeSO_4 \cdot H_2O$, CuO and Sb_2O_3. According to the characteristics of EN, the corrosion process of the BM, FGHAZ and ICHAZ could be divided into the initial passivation process and the following localized corrosion process. Passivation occurred on the surface of the CGHAZ initially and then turned into general corrosion. The corrosion strength of the BM, FGHAZ and ICHAZ decreased constantly with increasing corrosion time, while the corrosion strength of the CGHAZ decreased in the initial corrosion stage and then remained steady.

Keywords: Q315NS steel; heat-affected zone; H_2SO_4 solution; corrosion behaviour; electrochemical noise

1. INTRODUCTION

Dew point corrosion (DPC) is a serious corrosion phenomenon caused by condensed acid formed from corrosive gases (SO_3, HCl, NO_2, etc.) in power equipment for fossil fuels [1,2]. H_2SO_4 solution is the most common corrosive acid in DPC, and it is the most corrosive when the concentration of H_2SO_4 is in the range of 30-75 %. Q315NS steel is produced with an appropriate alloy design, and it is very suitable for those parts vulnerable to DPC in the power and petrochemical industries due to its excellent DPC resistance. As an indispensable process in the manufacture of the power and petrochemical industries, welding can change the corrosion behaviour, which is attributed to the welding thermal cycle [3-8]. The corrosion resistance of the heat-affected zone (HAZ) of Q315NS has an important effect on the safety and reliability of equipment produced with Q315NS. Thus, an investigation of the influence of the welding thermal cycle on the corrosion behaviour of Q315NS steel will be of great significance to the design of welding procedures.

Several methods, such as measurement of the mass loss, the polarization curves, electrochemical impedance spectra (EIS), and Mott-Schottky plots (MS), have been proposed to study corrosion processes [9-12]. Electrochemical noise (EN) measurement is a novel approach to investigate corrosion behaviour. EN, which was first described by Iversion in 1968 [13], refers to the spontaneous, random and nonequilibrium fluctuations of electrical signal that occur in electrochemical processes [14]. EN measurement has obvious advantages over traditional electrochemical methods, such as polarization and EIS. First, EN can provide more local electrochemical corrosion information while monitoring corrosion behaviour [15-18]. Second, an electrode process model does not need to be established during the analysis of corrosion behaviour using EN, which is more flexible [19]. Third, there is no need to bring an external potential or current signal into the electrochemical system in the EN measurement. An in situ monitoring of the corrosion process can be realized by EN measurement, which is capable of avoiding the external intervention of electrochemical measurement systems [20-25]. Recently, the EN measurement technique has been increasingly applied to electrochemical corrosion systems and has emerged as a promising method for corrosion analysis due to its obvious advantages [26-30]. Wang [28] investigated the corrosion process of 304 stainless steel in high temperature water and discussed the growth mechanisms of the oxide film using EN measurement. Yang [29] analysed the corrosion behaviour of carbon steel by EN measurement and EIS to reveal the mechanism of DPC. Huang [30] studied the corrosion behaviour of Q235 steel in 0.5 mol/L $NaHCO_3$/NaCl solution via EN measurement. The results showed that different states in corrosion could be identified by cluster analysis of the EN signal.

In this work, EN, polarization and EIS measurements of the base metal (BM) and HAZ of Q315NS steel in 50 wt.% H_2SO_4 solution at 25 °C were carried out. The fluctuation characteristics, power spectral density (PSD) and wavelet transform (WT) were employed to analyse the EN signal. The HAZ samples were prepared with a thermodynamic simulation technique, which was able to provide homogeneous HAZ samples. The present work aimed to investigate the corrosion process of the BM and HAZ of Q315NS steel in H_2SO_4 solution. Furthermore, efforts have been made to explore the influence of the welding thermal cycle on the corrosion mechanisms.

2. EXPERIMENTAL

2.1. HAZ Thermodynamic Simulation

Q315NS steel with composition (wt.%) C 0.06, Si 0.27, Mn 0.87, S 0.02, P 0.01, Ni 0.11, Mo 0.10, Cu 0.31, Sb 0.09 and Fe balance was used to prepare the simulated HAZ samples. The HAZ thermodynamic simulation experiments were performed in a Gleeble-3800 thermal-mechanical simulator (DSI, Poestenkill, NY, USA), which was capable of heating and cooling specimens at a high precision as set. The thermal cycle curves shown in Figure 1 were used to simulate the welding thermal cycle in the real welding process. In the HAZ thermodynamic simulation experiments, the simulated samples were heated to the peak temperature at a rate of 100 °C/s, held for 1 s and then cooled to 300 °C at the set cooling rate. The peak temperatures were set as 1320 °C, 930 °C and 830 °C, corresponding to the coarse-grained region (CGHAZ), fine-grained region (FGHAZ) and inter-critical region (ICHAZ), respectively. The weld input of 15 kJ/cm was chosen and the cooling time from 800 °C to 500 °C ($T_{8/5}$) was 15 s according to Equation (1) [31].

$$t_{8/5}=(0.043-4.3\times10^{-5}T_0)[1/(500-T_0)^2-1/(800-T_0)^2]Q^2\cdot F\cdot\delta^{-2} \quad (1)$$

where T_0 refers to the initial temperature of the sample, Q represents the welding heat input, and F and δ are the shape factor of the steel and the thickness, respectively.

The dimensions of the HAZ thermodynamic simulation specimens were 10 mm × 10 mm × 55 mm. Following the simulated thermal cycles, cuboid samples with a size of 10 mm × 10 mm × 6 mm were cut from the middle of the simulation samples and then used as HAZ specimens in the following measurements.

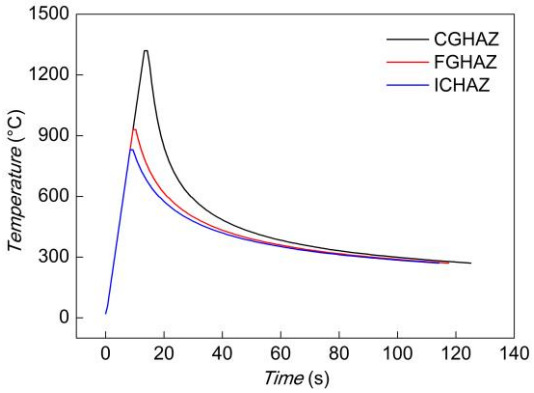

Figure 1. Thermal cycle curves in HAZ thermodynamic simulation experiments.

2.2. Microstructure Observation

The BM and HAZ specimens were ground with silicon carbide (SiC) abrasive paper to 2000 grit. Then these specimens were mechanically polished by flannelette and cleaned with ethanol in an ultrasonic bath for approximately 10 min. The microstructures of the BM and HAZ were observed using a Merlin Compact scanning electron microscope (SEM, Zeiss, Oberkochen, Ostalbkreis

Germany). In addition, the surface morphologies after being immersed in 50 wt. % H_2SO_4 solution for different time were observed using SEM.

2.3. Electrochemical Measurements

The electrochemical experiment samples were electrically connected with copper wires and then mounted in epoxy resin. After that the samples were ground SiC abrasive paper to 1200 grit, cleaned with ethanol in an ultrasonic bath for approximately 5 min and dried with cool air.

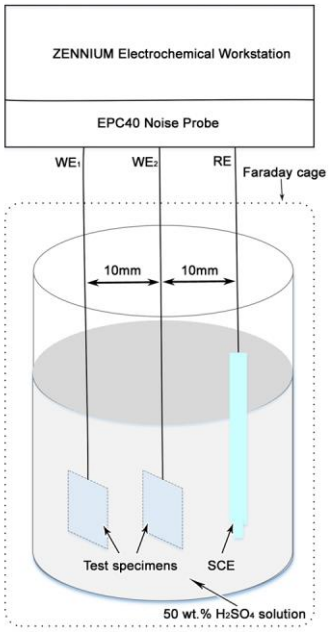

Figure 2. Schematic diagram of the electrode system for EN measurements.

A schematic of the electrode system for EN measurement is shown in Figure 2. The EN measurements were performed using a Zennium electrochemistry work station equipped with an EPC40 noise probe set (Zahner, Kronach, Bavaria, Germany). An EN measurements system with three electrodes was set up in which two identical test specimens, made from the BM or the simulated HAZ of Q315NS, were used as the working electrodes (WE), and the reference electrode (RE) was a saturated calomel electrode (SCE). The EN measurements were conducted with a data step width of 0.049 s, and the total measurement time was 6 h. The polarization and EIS measurements were carried out with a Zennium electrochemistry work station in a conventional three electrodes electrochemical system, in which a Pt plate and an SCE were used as the auxiliary electrode (AE) and RE, respectively. The measurements of polarization curves were conducted at a scan rate of 0.5 mV/s. The measurements of EIS were carried out within the 10^{-1} Hz to 10^{4} Hz frequencies. The area of the working electrode and the auxiliary electrode, which were exposed to the test electrolyte, was 10 mm × 10 mm. The electrolyte used in all electrochemical experiments was 50 wt.% H_2SO_4 solution with the temperature of 25 °C.

3. RESULTS AND DISCUSSION

3.1. Surface Observation

The SEM images of Q315NS steel and the simulated welding HAZ are shown in Figure 3. The BM of Q315NS steel exhibited a typical microstructure of polygonal ferrite (F) and pearlite (P), as shown in Figure 3(a). In the CGHAZ, as shown in Figure 3(b), granular bainite (GB) with coarse primary austenite grain boundaries could be observed. The bainite consisted of a bainitic ferrite matrix and the martensite/austenite constituents (M-A) as a second phase [32].

The final microstructure of the HAZ was largely determined by the applied welding thermal cycle and the austenite formation temperatures (A_{c1} and A_{c3}). The A_{c1} and A_{c3} of Q315NS were 721 °C and 909 °C, respectively. The CGHAZ experienced complete austenization in the heating stage due to the high peak temperature (1320 °C) of the welding thermal cycle. In addition, the austenite grain was coarse, which was the result of the long stay time above A_{c1}. The bainitic transformation occurred in the cooling stage and GB with coarse grains finally formed.

The austenitic transformation occurred during the heating stage of the FGHAZ and ICHAZ because the peak temperatures were above A_{c1}. Then, austenite transformed to pearlite and ferrite in the cooling stage. As a result, the microstructure of pearlite and ferrite was observed in the FGHAZ and ICHAZ, similar to that of the BM. In addition, the average grain size of the FGHAZ was smaller than that of the BM, which was due to the fast cooling rate during the transformation from austenite to pearlite and ferrite. The grain size of the ICHAZ was almost the same as that of the BM. The difference among the grain sizes of the BM, FGHAZ, and ICHAZ was mainly determined by the peak temperature that they experienced.

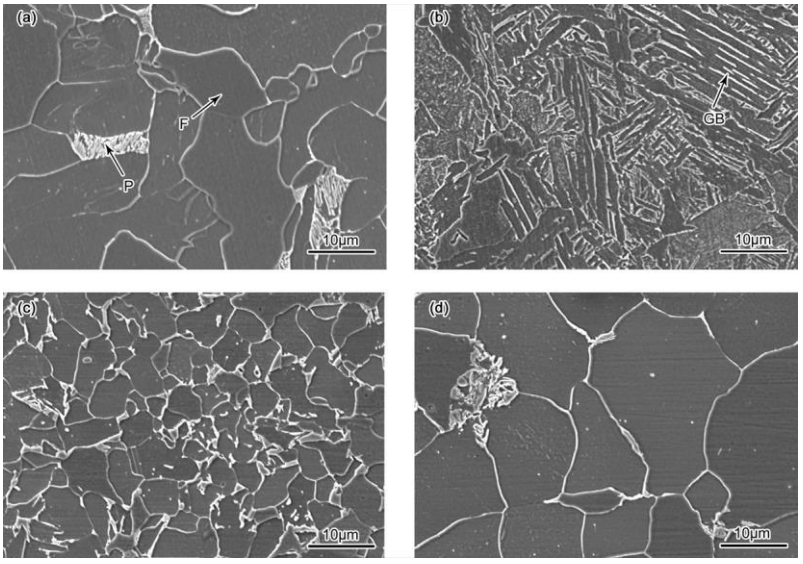

Figure 3. SEM images of (a) the BM, (b) the CGHAZ, (c) the FGHAZ and (d) the ICHAZ of Q315NS.

The surface morphologies of the BM, CGHAZ, FGHAZ and ICHAZ immersed in 50 wt.% H_2SO_4 solution for 12 h are shown in Figure 4. As shown in Figure 4(a), the BM surface was mainly

covered with dense corrosion product film, which mainly covered the ferrite region. In addition, there were some microvoids rather than dense film in the pearlite region, which may be due to the preferential growth of the corrosion product [34]. The corrosion product film was able to inhibit the corrosion process while the microvoids played a negative role. Meanwhile, the microvoids indicated that a localized corrosion process occurred. The corrosion process of the FGHAZ and ICHAZ should be similar to that of the BM according to the similar surface morphologies. The corrosion product film formed on the surface of the CGHAZ was uniform, loose and rough, as shown in Figure 4(b). The uniform corrosion product film indicated that the CGHAZ electrode underwent general corrosion. In addition, the film formed on the surface of the CGHAZ was rougher and looser than that of the BM, although there were no microvoids.

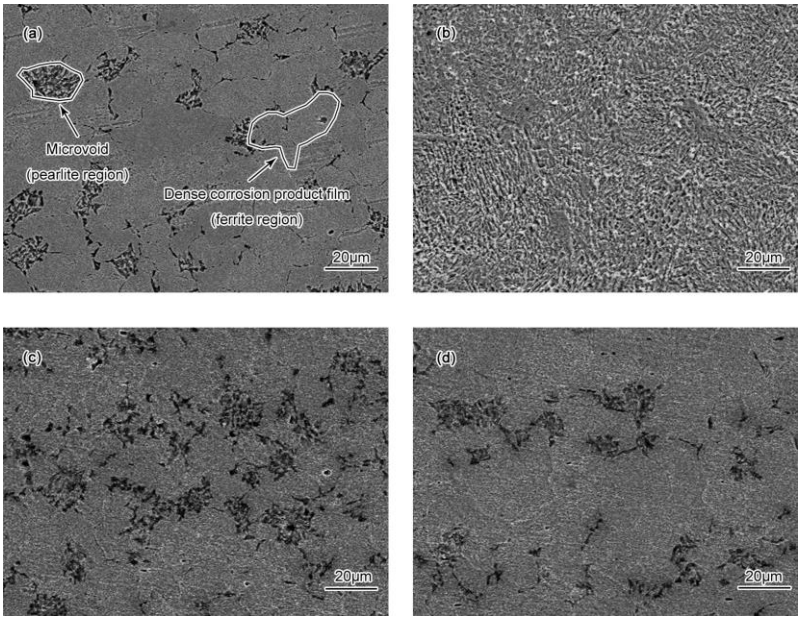

Figure 4. SEM images of (a) the BM, (b) the CGHAZ, (c) the FGHAZ and (d) the ICHAZ after 12 h immersion in 50 wt.% H_2SO_4 solution.

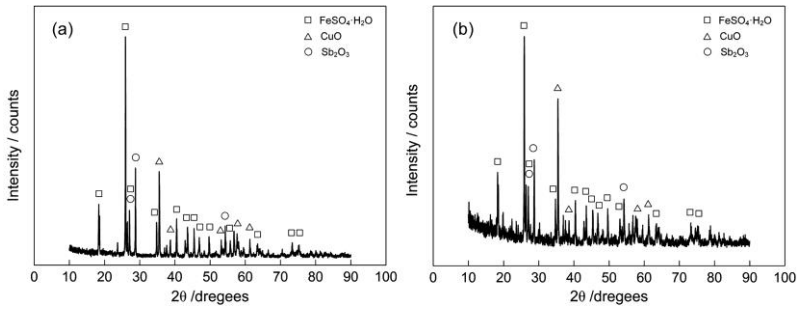

Figure 5. XRD patterns of the corrosion products of (a) the BM and (b) the CGHAZ after 12 h immersion in 50 wt.% H_2SO_4 solution.

The X-ray diffraction (XRD) patterns of the corrosion products of the BM and CGHAZ after 12 h of immersion in 50 wt.% H_2SO_4 solution, as shown in Figure 5, indicated that the corrosion products

of the BM and CGHAZ were both composed of the major $FeSO_4 \cdot H_2O$ and a slight amount of CuO and Sb_2O_3. There was no obvious difference between the BM and CGHAZ in the corrosion product phase.

3.2. The Characteristics of EN Time Records

It has been confirmed that DC drift of the EN signal can cause serious errors in the results of analysis [35], and the moving average removal method (MAR) proposed by Tan can remove the DC drift [36-38]. Thus, the DC drifts in EN records were removed by the MAR before the analysis. The EN records of BM and HAZ samples after different immersion times are shown in Figure 6 to Figure 9. The fluctuations of EN records can reveal the corrosion behaviour of electrodes in detail.

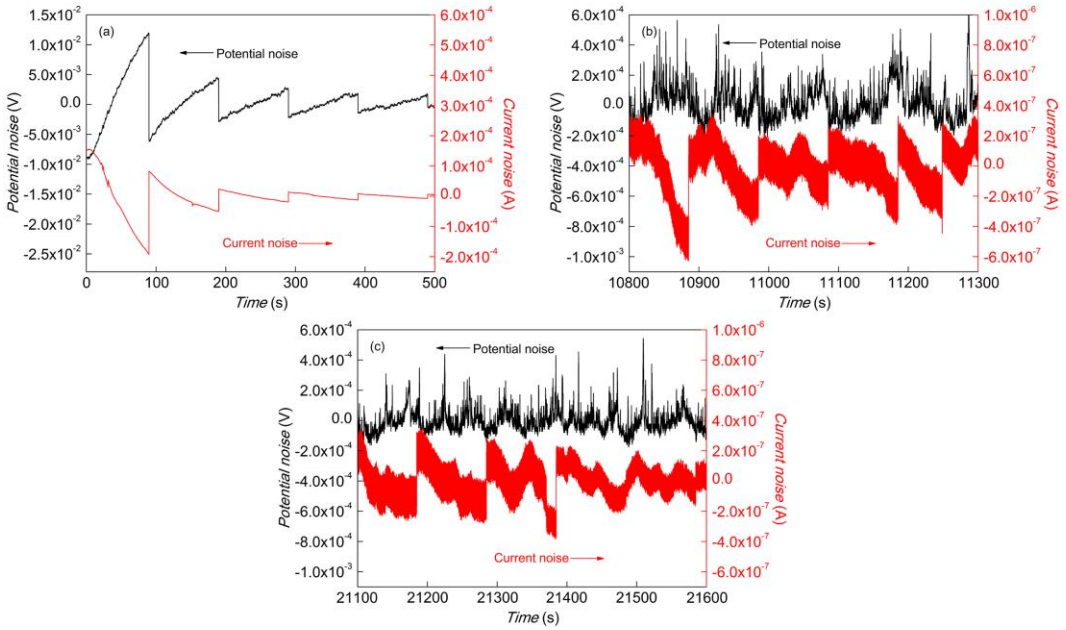

Figure 6. EN time records of the BM immersed in 50 wt.% H_2SO_4 solution for (a) 0-500 s, (b) 10800-11300 s and (c) 21100-21600 s.

As shown in Figure 6(a), the electrochemical potential noise (EPN) fluctuations were characterized by a sudden drop and then a slow rise, while the electrochemical current noise (ECN) increased slowly and then suddenly decreased in the initial corrosion stage. Generally, the sharp rise and slow decline of the ECN corresponded to the breakdown and repassivation of the passive film, while the slow rise after the sudden drop of the EPN was related to the charge/discharge on the electrode surface [39]. These fluctuations of EN records in the initial corrosion stage meant that a passivation process occurred. In addition, the fluctuation range decreased regularly over the corrosion time, which indicated that the passivation process weakened gradually. This pattern lasted for approximately 1500 s. Then, some sudden rises accompanied by many fast and small fluctuations could be found in the ECN, while only fast and small fluctuations were observed in the EPN, as shown in Figure 6(b) and Figure 6(c). The large number of fast and small fluctuations shown in both the EPN and ECN indicated that diffusion occurred on the surface. However, it could be inferred from the

sudden rise of the ECN that breakdown of the passive film occurred, which might be a feature of localized corrosion. There was no slow rise of potential because the passive film covered most regions and the charge/discharge process on small areas (imperfect passivation regions) had no obvious effect on the potential of the capacitance. The fluctuation amplitudes of the ECN and EPN both decreased with time in this stage, which meant that the corrosion strength decreased as the corrosion time was prolonged. From the fluctuations of EN records of the BM, it was deduced that the initial passivation process turned into localized corrosion and that the corrosion strength increased as time went on. In general, metastable pitting and localized corrosion occurred in non-oxidizing acid [40], while a passivation process occurred in 50 wt.% H_2SO_4 solution due to strong oxidization.

Figure 7 shows the fluctuations of EN records of the CGHAZ in different periods. In the initial corrosion stage of the CGHAZ, approximately from the beginning to 1200 s, the characteristic of EN records was similar to that for the BM. This result implied that a passivation process also took place on the surface of the CGHAZ in this corrosion stage. However, there were small quantities of small fluctuations both in the ECN and EPN, which were different from those of the BM. This result meant that there might be differences in the passivation process and passive film structure between the CGHAZ and BM. After the initial corrosion stage, there were only many fast and small fluctuations in both the ECN and EPN, which was the obvious feature of general corrosion [14,39,41]. Furthermore, the fluctuation amplitudes of the ECN and EPN were almost the same, which indicated that the corrosion strength did not change significantly in this corrosion stage.

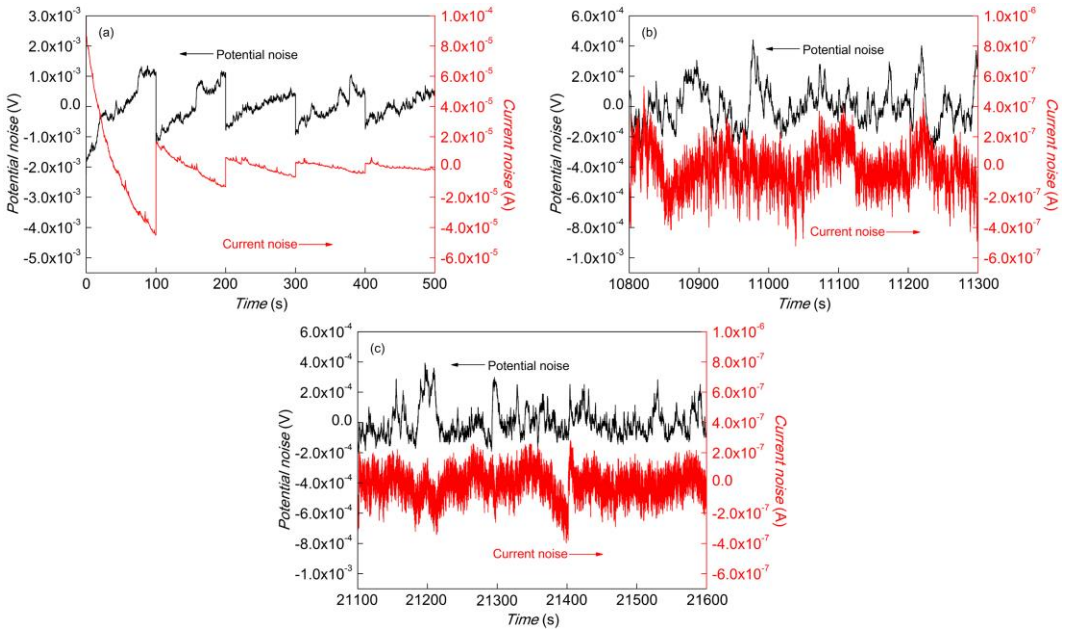

Figure 7. EN time records of the CGHAZ immersed in 50 wt.% H_2SO_4 solution for (a) 0-500 s, (b) 10800-11300 s and (c) 21100-21600 s.

Figure 8 and Figure 9 show the fluctuations of EN records of the FGHAZ and ICHAZ. It could be inferred that the FGHAZ and ICHAZ electrodes underwent a corrosion process similar to that for the BM according to the fluctuation characteristics, which were similar to those of the BM. The corrosion behaviour according to the EN of Q315NS agreed well with the surface observations above.

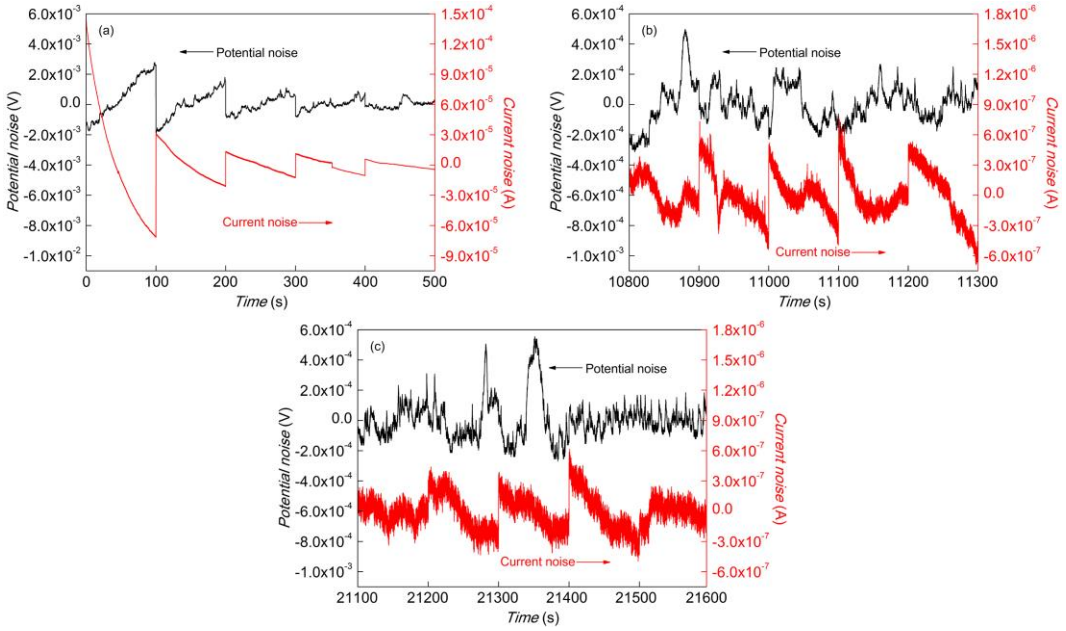

Figure 8. EN time records of the FGHAZ immersed in 50 wt.% H_2SO_4 solution for (a) 0-500 s, (b) 10800-11300 s and (c) 21100-21600 s.

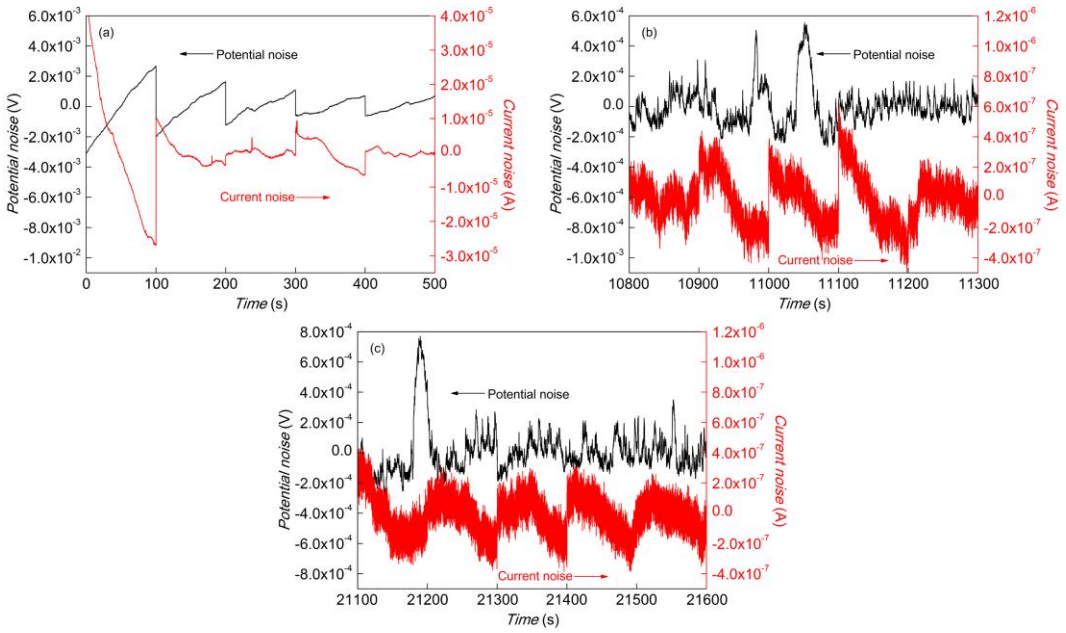

Figure 9. EN time records of the ICHAZ immersed in 50 wt.% H_2SO_4 solution for (a) 0-500 s, (b) 10800-11300 s and (c) 21100-21600 s.

3.3. Power Spectral Density

The noise power spectral density (*PSD*) plot, as one of the most useful analysis methods for EN data, can reveal the corrosion mechanism of the electrode. The *PSD* is calculated as follows [42]:

$$\lg PSD = A + S \lg f \quad (2)$$

where *A* is the noise intensity and *S* is the slope of the straight-line region (high frequency section).

Some studies have suggested that the *PSD* parameters *A* and *S* of EPN are related to the corrosion process [43,44]: the more positive the value of *S* is, the more easily pitting corrosion initiates; the higher the value of *A* is, the more serious the corrosion is. In other words, the *S* and *A* of *PSD* plots have been proposed as indicators of the corrosion type and the corrosion rate, respectively. The *PSD* plots of the EPN of test electrodes for different corrosion times are shown in Figure 10, which were obtained by applying the fast Fourier transform (FFT). The parameters of the *PSD* plots are summarized in Table 1.

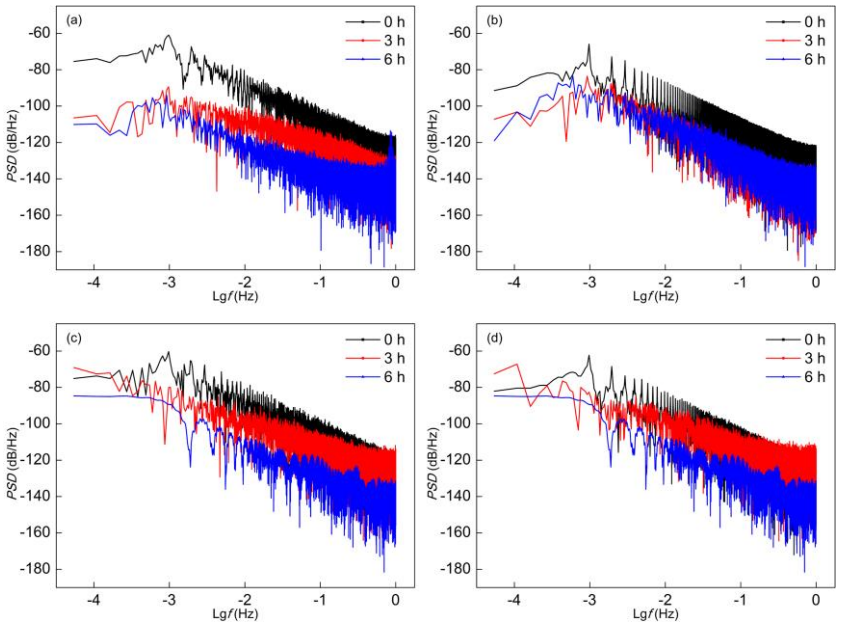

Figure 10. PSD plots of (a) the BM, (b) the CGHAZ, (c) the FGHAZ and (d) the ICHAZ after immersion in 50 wt.% H_2SO_4 solution.

Table 1. PSD parameters of the test electrodes after immersion in 50 wt.% H_2SO_4 solution for different time.

Electrodes	Immersion time (h)	Potential noise	
		A (dB/Hz)	*K* (dB/Hz^2)
BM	0	-127.85	-17.81
	3	-139.99	-16.23
	6	-148.60	-12.31
CGHAZ	0	-129.74	-16.45
	3	-148.35	-16.62
	6	-146.84	-17.24
FGHAZ	0	-129.44	-16.96
	3	-141.95	-13.88
	6	-146.42	-12.04
ICHAZ	0	-132.31	-16.12
	3	-135.76	-13.43
	6	-136.18	-13.18

Figure 10(a) shows the *PSD* plots of the BM after different corrosion times. The value of *A* was approximately -127.85 dB/Hz at the beginning of corrosion, reduced to -139.99 dB/Hz after 3 h, and then reduced to -148.60 dB/Hz after 6 h. The decrease of *A* indicated that the corrosion strength weakened incrementally over time, which may be due to the contribution of the passive film and the corrosion products attached to the electrode surface. Meanwhile, the value of *S* was -17.81 dB/Hz^2 in the initial corrosion stage, increased to -16.23 dB/Hz^2 after 3 h, and then constantly increased to -12.31 dB/Hz^2 after 6 h. The increase of *S* implied that the localized corrosion tendency was enhanced, which may be due to the corrosion of imperfect passivation regions as well as the erosion of the passive film by sulfate ions [45]. With the increase of corrosion time, the imperfect passivation regions were more prone to erosion, giving rise to the enhancement of the localized corrosion tendency.

Figure 10(b) shows the *PSD* plots of the CGHAZ after different corrosion times. The value of *A* decreased from -129.74 dB/Hz to -148.35 dB/Hz during the first 3 h, and then became -146.84 dB/Hz. The variation of *A* indicated that the corrosion rate decreased in the initial corrosion stage and then remained nearly constant with increasing immersion time. The value of *S* slowly increased from -16.45 dB/Hz^2 to -17.24 dB/Hz^2, which showed no significant difference.

The variations in the *PSD* parameters of the FGHAZ and ICHAZ, as shown in Table 1, were similar to those of the BM. This implied that the FGHAZ and ICHAZ underwent a corrosion process similar to that for the BM.

3.4. Wavelet Transform

Wavelet transform (WT) is a widely used analysis method to detect, classify and discriminate transient signals. Recently, WT has been used to analyse EN data and is able to provide useful information about the dominant corrosion process [46]. The associated corrosion events are interpreted by a set of wavelet energies, which contain information on the time-scale characteristics. The time-scale of the corrosion event is related to the corrosion process: a faster corrosion process corresponds to a smaller time-scale. As a result, the dominant corrosion process can be qualitatively and quantitatively distinguished by the wavelet energy distribution plot (EDP). Generally, the relative wavelet energy distribution in crystals *D*1-*D*3, *D*4-*D*6 and *D*7-*D*8 are mainly relate to the corrosion processes of metastable pitting, localized corrosion and diffusion when the time-scales of crystal *D* are ranked from *D*1 to *D*8 [47-50]. The EDPs corresponding to the EPN of the BM and CGHAZ are shown in Figure 11.

As shown in Figure 11(a), the wavelet energy of the BM electrode mainly accumulated in crystals *D*7-*D*8 during the initial corrosion stage, which revealed that the corrosion on the electrode surface was mainly dominated by a long time-scale process related to the diffusion process. This long time-scale process suggested that the electrode surface had undergone the passivation process at the beginning of corrosion [28,51]. Approximately 0.5 h later, the vast majority of the energy distribution was in crystals *D*4-*D*8, which demonstrated that localized corrosion and diffusion occurred on the electrode surface. The reason why there was a localized corrosion process after the passivation process might be that parts of the BM surface were not passivated well or covered with a protective film. In

other words, localized corrosion occurred in regions that were not covered with a dense corrosion product film.

Figure 11(b) shows the EDP corresponding to the EPN of the CGHAZ. It can be concluded from Figure 11(b) that the wavelet energy distribution was dominated by low frequency energy (crystals D7-D8), implying that diffusion was the major process in the corrosion of the CGHAZ. It was demonstrated that general corrosion occurred throughout the corrosion of the CGHAZ.

Figure 11(c) and Figure 11(d) show similar wavelet energy distributions to Figure 11(a), which might indicate that the FGHAZ and ICHAZ electrodes underwent a corrosion process similar to that for the BM.

The wavelet energy was mainly dominated by the fast frequency energy in the initial corrosion stage in HCl solution, corresponding to a metastable pitting process [40]. However, a passivation process occurred first in 50 wt.% H_2SO_4 solution because it was a strong oxidizing acid.

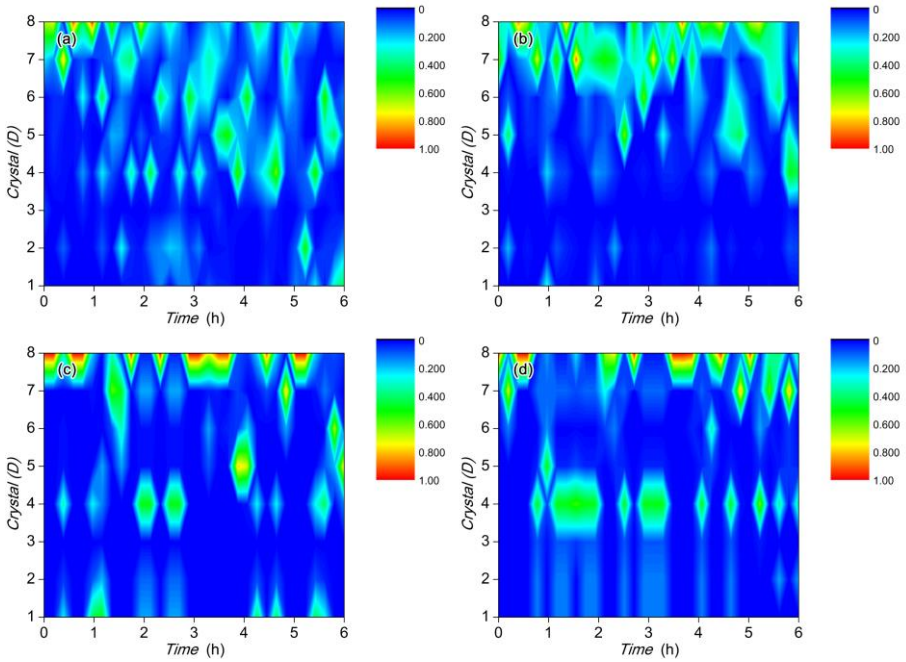

Figure 11. EDP of the BM and HAZ immersed in 50 wt.% H_2SO_4 solution: (a) BM; (b) CGHAZ; (c) FGHAZ; (d) ICHAZ.

3.5. Polarization and EIS

Some authors have reported that the EN is much useful for studying the corrosion process, particularly when it is used in conjunction with polarization, EIS and other electrochemical techniques [52-54]. In this work, polarization and EIS measurements were carried out.

Figure 12 shows the polarization curves of the BM and HAZ in 50 wt.% H_2SO_4 solution at 25 °C. The cathodic polarization curves of the electrodes had nearly the same shapes and slopes, indicating that a similar cathodic polarization process occurred in all test electrodes. Generally, the cathodic polarization process of steel involves the formation of hydrogen in acid solution. In the anodic polarization process, the current density of all electrodes increased rapidly when the potential

first increased. With continuously increasing potential, the anode current density decreased sharply and then approached a stable value. This result indicated that the passive process occurred in this stage, which was conducive to preventing further corrosion. However, the anodic polarization curves of the CGHAZ, FGHAZ and ICHAZ were more positive compared with the polarization curve of the BM, which indicated that the reactions of HAZ electrodes were affected by welding thermal cycles. In other words, the welding thermal cycle affected the passive process of the HAZ and the structure of the passive film. In particular, the polarization curve of the CGHAZ showed the most positive potential and the highest passive current density. It could be concluded that the passivation process of the CGHAZ was affected the most due to the highest peak temperature being reached in the welding thermal cycle.

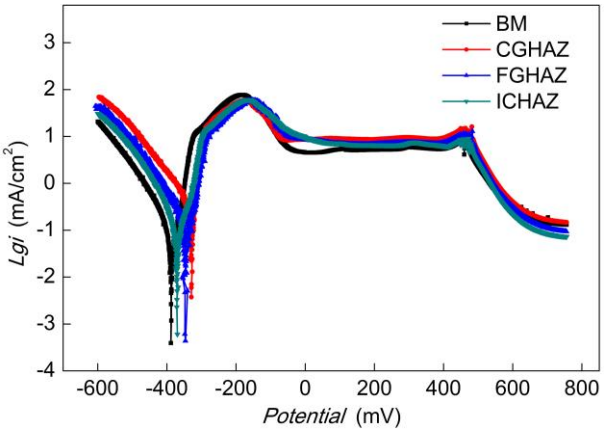

Figure 12. Polarization curves for the test electrodes immersed in 50 wt.% H_2SO_4 solution.

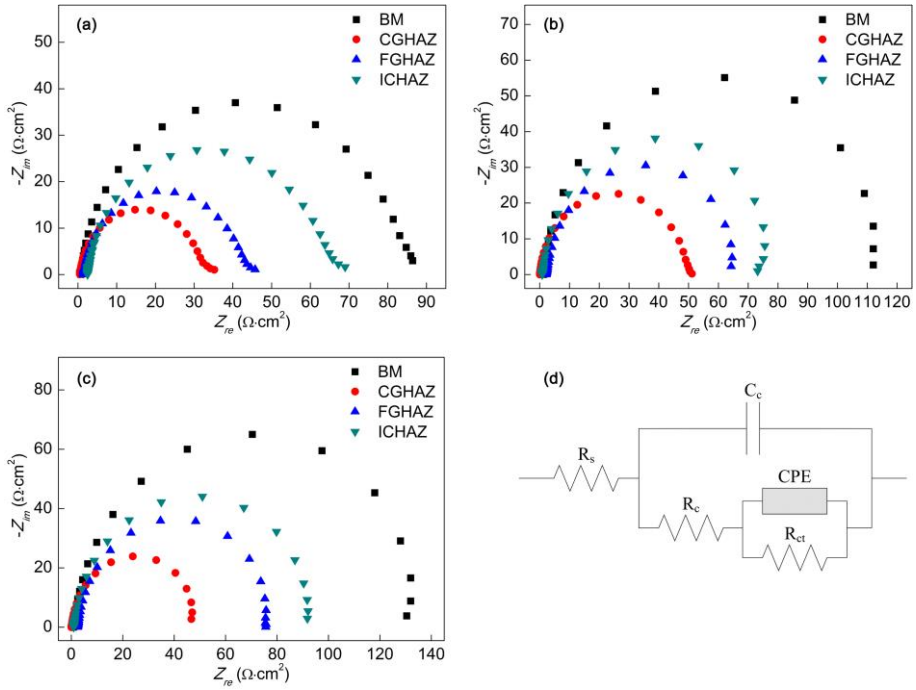

Figure 13. Nyquist plots for the test electrodes immersed in 50 wt.% H_2SO_4 solution for (a) 0 h, (b) 3 h, (c) 6 h and (d) the corresponding equivalent circuit.

Figure 13 shows the Nyquist plots of test electrodes (BM, CGHAZ, FGHAZ and ICHAZ) after different immersion times in 50 wt.% H_2SO_4 solution and the corresponding equivalent circuit which was used to fit the electrochemical system in the corrosion process [55,56]. All Nyquist plots were characterized by one capacitive arc in the high frequency zone, which implied that the corrosion was mostly dominated by the charge transfer process. In addition, the diameter of all Nyquist plots increased with immersion time, which meant that the corrosion resistance increased with time. The Nyquist plots of the BM showed the maximum diameter, while the Nyquist plots of the CGHAZ showed the minimum, which indicated that the corrosion resistance of the BM was the maximum and the corrosion resistance of the CGHAZ was the smallest.

Table 2. EIS parameters for the test electrodes immersed in 50 wt.% H_2SO_4 solution for different times.

Specimens	Immersion time (h)	R_{sol} ($\Omega \cdot cm^{2)}$	C_c (μF)	R_c ($\Omega \cdot cm^2$)	R_{ct} ($\Omega \cdot cm^{2)}$	CPE	
						Y ($S \cdot sn/cm^2$)	n
BM	0	1.004E-13	1.177	0.947	81.86	6.966E-5	0.9628
	3	1.395E-7	0.7411	1.515	114.30	5.956E-4	0.9559
	6	9.751E-8	1.0840	0.9164	137.1	3.604E-4	0.9381
CGHAZ	0	9.924E-8	1.929	0.669	31.38	1.381E-4	0.9719
	3	2.287E-7	5.594	0.3803	49.13	3.417E-4	0.9684
	6	1.355E-9	5.629	0.3989	49.41	8.757E-4	0.9556
FGHAZ	0	7.662E-7	0.4751	1.576	41.24	5.826E-5	0.9391
	3	4.408E-7	0.4666	2.373	66.13	7.793E-4	0.9315
	6	6.139E-7	0.4404	2.921	73.96	4.438E-4	0.9751
ICHAZ	0	9.571E-8	0.2447	2.681	62.06	4.027E-5	0.9349
	3	2.540E-7	1.123	0.9533	77.57	6.213E-4	0.9489
	6	2.533E-7	1.060	1.001	93.72	4.678E-4	0.9445

The EIS parameters, which are calculated according to the equivalent circuit shown in Figure 13(d), are shown in Table 2. R_s, R_c and R_{ct} represent the resistance of solution, the resistance of the corrosion product and the charge transfer resistance, respectively. C_c stands for the capacitance of the corrosion product and a constant phase element (CPE) is used to describe the double electrical layer of the interface between the electrode and the electrolyte [57]. The R_{ct} of all electrodes at any corrosion stage was greater than R_c and R_s, which again implied that the corrosion of all electrodes in 50 wt.% H_2SO_4 solution was mainly controlled by the charge transfer process [58,59]. The increase of R_{ct} for the BM, FGHAZ and ICHAZ throughout the overall corrosion process indicated that the inhibiting effect on the transportation of ions and charges was enhanced. This might be due to the corrosion product formed on the surface, which increased the electrochemical reaction impedance and improved the corrosion resistance [55]. The R_{ct} of the CGHAZ increased from 31.38 $\Omega \cdot cm^2$ to 49.13 $\Omega \cdot cm^2$ in the first 3 h and then remained constant, which meant that the passive process in the initial corrosion stage prevented corrosion effectively and that the inhibiting effect was then no more effective with corrosion

time. The C_c is closely connected with the morphology of the corrosion product. A rougher corrosion product film leads to a higher value of C_c [56]. The CGHAZ exhibited the roughest corrosion product film according to the highest C_c throughout the entire corrosion process. There was no obvious difference in the value of C_c among the BM, FGHAZ and ICHAZ, which meant that the corrosion product film morphologies of these electrodes were similar. The admittance of CPE (Y) of the CGHAZ became larger, from 1.381×10^{-4} S·sn/cm^2 to 8.757×10^{-4} S·sn/cm^2, while the Y of the other electrodes rose in the first 3 h and then decreased. This might be the result of the difference in the corrosion process between the CGHAZ and the other electrodes.

It could be presumed that there were some differences in the morphology of corrosion product film and the structure of electrical double layer between the CGHAZ and the other samples (BM, FGHAZ and ICHAZ). The CGHAZ electrode showed a rougher corrosion product film and a lower charge transfer resistance. In other words, the CGHAZ electrode showed the worst corrosion resistance, while the BM electrode showed the best corrosion resistance. The analysis results of polarization and EIS were consistent with those of EN analysis.

4. CONCLUSIONS

The corrosion behaviours and mechanism of Q315NS steel and the HAZ in 50 wt.% H_2SO_4 solution at 25 °C were investigated based on EN. The main conclusions are as follows:

(1) The microstructure in the BM, FGHAZ and ICHAZ of Q315NS steel was mainly pearlite and ferrite, while the CGHAZ mainly consisted of granular bainite owing to the high peak temperature of the welding thermal cycle.

(2) A dense corrosion product film was formed on the ferrite region of the BM, FGHAZ and ICHAZ, while there were some microvoids on the pearlite region of these samples. The surface of the CGHAZ was covered with uniform, loose and rough corrosion product film. The corrosion products of the BM and CGHAZ were both mainly composed of $FeSO_4\cdot H_2O$, CuO and Sb_2O_3.

(3) The corrosion processes of the BM, FGHAZ and ICHAZ were similar, and the overall corrosion process could be described as two stages: the first stage involved the passivation process, and the second stage corresponded to localized corrosion. However, on the surface of the CGHAZ, passivation occurred in the initial stage, and then the corrosion process turned into general corrosion.

(4) The corrosion strength of the BM, FGHAZ and ICHAZ constantly decreased over time. The corrosion strength of the CGHAZ decreased at the beginning of corrosion and then approached stability. The corrosion resistance of the HAZ was in roughly negative correlation to the peak temperature of the welding thermal cycle.

ACKNOWLEDGMENTS

This work was supported by the Natural Scientific Research Innovation Foundation in Harbin Institute of Technology [No.HIT.NSRIF.201703] and the Shandong Provincial Natural Science Foundation of China [No.ZR2016EEQ03].

References

1. R. Ebara, F. Tanaka, M. Kawasaki, *Eng. Fail. Anal.,* 33 (2013) 29.
2. B. Zarenezhad, A. Aminian, *Energy Convers. Manage.,* 52 (2011) 911.
3. J.S. Wei, Y.C. Qi, Z.L. Tian, Y. Peng, *J. Iron Steel Res. Int.,* 23 (2016) 955.
4. H.L. Ming, Z.M. Zhang, P.Y. Xiu, J.Q. Wang, E.H. Han, W. Ke, M.X. Su, *Acta Metall. Sin.,* 26 (2016) 848.
5. L.J. Dong, Q.J. Peng, E.H. Han, W. Ke, L. Wang, *Corros. Sci.,* 107 (2016) 172.
6. J.Y. Zhu, L.N. Xu, Z.C. Feng, G.S. Frankel, M.X. Lu, W. Chang, *Corros. Sci.,* 111 (2016) 391.
7. J. Verma, R.V. Taiwade, *J. Manuf. Process.,* 14 (2016) 1.
8. G.A. Zhang, Y.F. Cheng, *Electrochim. Acta,* 55 (2009) 316.
9. J. Xu, X.Q. Wu, E.H. Han, *Electrochim. Acta,* 71 (2012) 219.
10. H. Sun, X.Q. Wu, E.H. Han, *Corros. Sci.,* 59 (2012) 334.
11. H. Sun, X.Q. Wu, E.H. Han, *Corros. Sci.,* 51 (2009) 2840.
12. H. Sarlak, M. Atapour, M. Esmailzadeh, *Mater. Des.,* 66 (2015) 209.
13. S. Girija, U. K. Mudali, V.R. Raju, R.K. Dayal, H.S. Khatak, B. Raj, *Mater. Sci. Eng. A,* 407 (2005) 188.
14. U. Bertocci, F. Huet, *Corros.,* 51 (1995) 131.
15. N. Du, W.M. Tian, Q. Zhao, S.B. Zhao, *Acta Metall. Sin.,* 48 (2012) 807.
16. Y.F. Wang, G.X. Cheng, *Mater. Des.,* 94 (2016) 176.
17. B.P. Markhali, R. Naderi, M. Mahdavian, *J. Electroanal. Chem.,* 714-715 (2014) 56.
18. X.L. Liu, T. Zhang, Y.W. Shao, G.Z. Meng, F.H. Wang, *Corros. Sci.,* 52 (2010) 892.
19. J.O. Okeniyi, C.A. Loto, A.P.I. Popoola, *Metals,* 6 (2016) 255.
20. C.L. Zeng, W. Wang, W.T. Wu, *Oxid. Met.,* 53 (2000) 289.
21. A. Aballe, M. Bethencourt, F.J. Botana, M. Marcos, *Electrochim. Acta,* 44 (1999) 4805.
22. R. Morales, A. Albiter, M. Salazar, F.J. Tavera, R. Escudero, J.G. Gonzalez-Rodriguezc, *Mater. Sci. Eng. A,* 397 (2005) 1.
23. A. Chira,B. Bucur, G.L. Radu, *Mater.,* 10 (2017) 235.
24. E. Budevski, W. Obretenov, W. Bostanov, G. Staikov, J. Doneit, K. Jüttner, W.J. Lorenz, *Electrochim. Acta,* 34 (1989) 1023.
25. J.F. Chen, W.F. Bogaerts, *Corros.,* 52 (1996) 753.
26. Y. Puget, K. Trethewey, R.J.K. Wood, *Wear,* 233 (1999) 552.
27. Z. Zhang, W.H. Leng, Q.Y. Cai, F.H. Cao, J.Q. Zhang, *J. Electroanal. Chem.* 578 (2005) 357.
28. K. Wang, J.H. Wang, W.B. Hu, *Mater. Des.,* 82 (2015) 155.
29. Y.G. Yang, T. Zhang, Y.W. Shao, G.Z. Meng, F.H. Wang, *Corros. Sci.,* 71 (2013) 62.
30. J.Y. Huang, X.P. Guo, Y.B. Qiu, Z.Y. Chen, *Electrochim. Acta,* 53 (2007) 680.
31. W.Y. Zhang, Welding Metallurgy (Basic Principle), China Machine Press, (1996) Beijing, China.
32. Z.Q. Cui, B.X. Liu, Metallurgy and Treatment Theory, Third ed., Harbin Institute of Technology Press, (2007) Harbin, China.
33. L.W. Wang, Z.Y. Liu, Z.Y. Cui, C.W. Du, X.H. Wang, *Corros. Sci.,* 85 (2014) 401.
34. S.Q. Zhang, H.Y. Zhao, F.Y. Shu, W.X. He, G.D. Wang, *Metals,* 7 (2017) 194.
35. R.A. Cottis, *Corros.,* 57 (2001) 265.
36. Y.J. Tan, S. Bailey, B. Kinsella, *Corros. Sci.,* 38 (1996) 1681.
37. F.Z. Mansfeld, Z. Sun, C.H. Hsu, *Electrochim. Acta,* 46 (2001) 3651.
38. U. Bertocci, F. Huet, P. Rousseau, R.P. Nogueira, *Corros.,* 58 (2002) 337.
39. Y.F. Cheng, M. Wilmott, J.L. Luo, *Corros. Sci.,* 41 (1999) 1245.
40. S. Q. Zhang, H. Y. Zhao, F. Y. Shu, G. D. Wang, B. Liu and B. S. Xu, *RSC Adv.,* 8 (2018) 454.
41. H. Sarlak, M. Atapour, M. Esmailzadeh, *Mater. Des.,* 66 (2015) 209.
42. L. Liu, Y. Li, F.H. Wang, *Electrochim. Acta* ,54 (2008) 768.
43. Y.F. Cheng, B.R. Rairdan, J.L. Luo, *J. Appl. Electrochem.,* 28 (1998) 1371.

44. Z. Zhang, J.Q. Zhang, J.M. Wang, N.C. Chu, *Chin. J. Nonferrous Met.*, 101 (2001) 284.
45. Z.Y. Liu, C.F. Dong, Z.J. Jia, X.G. Li, *Acta Metall. Sin.*, 47 (2011) 1009.
46. P. Planinsic, A. Petek, *Electrochim. Acta*, 53 (2008) 5206.
47. A.M. Homborg, T. Tinga, X. Zhang, E.P.M.V. Westing, P.J. Oonincx, G.M. Ferrari, J.H.W.D. Wit, J.M.C. Mol, *Electrochim. Acta*, 104 (2013) 84.
48. M.J. Bahrami, M. Shahidi, S.M.A. Hosseini, *Electrochim. Acta*, 148 (2014) 127.
49. F.H. Cao, Z. Zhang, J.X. Su, Y.Y. Shi, J.Q. Zhang, *Electrochim. Acta*, 51 (2006) 1359.
50. L.J. Zhang, Z. Zhang, J.Q. Zhang, *Acta Phys.-Chim. Sin.*, 24 (2008) 1831.
51. Y.Y. Shi, Z. Zhang, J.X. Su, F.H. Cao, J.Q. Zhang, *Electrochim. Acta*, 51 (2006) 4977.
52. J. Mojica, E. García, F.J. Rodríguez, J. Genescá, *Prog. Org. Coat.*, 42 (2001) 218.
53. M.G. Pujar, N. Parvathavarthini, R.K. Dayal, S. Thirunavukkarasu, *Corros. Sci.*, 51 (2009) 1707.
54. A. Ehsani, M.G. Mahjani, M. Hosseini, R. Safaria, R. Moshrefi, H.M. Shiri, *J. Colloid Interface Sci.*, 490 (2017) 444.
55. X.X. Wang, Y.M. Gao, K. Li, J.B. Yan, Y.F. Li, J.B. Feng, *Corros. Sci.*, 69 (2013) 369.
56. X.X.Wang, Y.M. Gao, Y.F. Li, T. Yang, *Corros. Sci.*, 87 (2014) 211.
57. K. Jüttner, *Electrochim. Acta*, 35 (1990) 1501.
58. Q.B. Zhang, Y.X. Hua, *Electrochim. Acta*, 54 (2009) 1881.
59. M.E. Achouri, S. Kertit, H.M. Gouttaya, B. Nciri, Y. Bensouda, L. Perez, M.R. Infante, K. Elkacemi, *Prog. Org. Coat.*, 43 (2001) 267.